Cyclophanes Hot Paper

How to cite: *Angew. Chem. Int. Ed.* **2022,** *61,* e202208679
International Edition: doi.org/10.1002/anie.202208679
German Edition: doi.org/10.1002/ange.202208679

Aggregation-Induced Emission and Circularly Polarized Luminescence Duality in Tetracationic Binaphthyl-Based Cyclophanes

*Amine Garci[+], Seifallah Abid[+], Arthur H. G. David, Marcos D. Codesal, Luka Đorđević, Ryan M. Young, Hiroaki Sai, Laura Le Bras, Aurélie Perrier, Marco Ovalle, Paige J. Brown, Charlotte L. Stern, Araceli G. Campaña, Samuel I. Stupp, Michael R. Wasielewski, Victor Blanco, and J. Fraser Stoddart**

Abstract: Here, we report an approach to the synthesis of highly charged enantiopure cyclophanes by the insertion of axially chiral enantiomeric binaphthyl fluorophores into the constitutions of pyridinium-based macrocycles. Remarkably, these fluorescent tetracationic cyclophanes exhibit a significant AIE compared to their neutral optically active binaphthyl precursors. A combination of theoretical calculations and time-resolved spectroscopy reveal that the AIE originates from limited torsional vibrations associated with the axes of chirality present in the chiral enantiomeric binaphthyl units and the fine-tuning of their electronic landscape when incorporated within the cyclophane structure. Furthermore, these highly charged enantiopure cyclophanes display CPL responses both in solution and in the aggregated state. This unique duality of AIE and CPL in these tetracationic cyclophanes is destined to be of major importance in future development of photonic devices and bio-applications.

[*] Dr. A. Garci,[+] Dr. S. Abid,[+] Dr. A. H. G. David, Dr. L. Đorđević, Prof. R. M. Young, Dr. H. Sai, M. Ovalle, P. J. Brown, Dr. C. L. Stern, Prof. S. I. Stupp, Prof. M. R. Wasielewski, Prof. J. F. Stoddart
Department of Chemistry, Northwestern University
2145 Sheridan Road, Evanston, IL 60208 (USA)
E-mail: stoddart@northwestern.edu

M. D. Codesal, Dr. A. G. Campaña, Dr. V. Blanco
Departamento de Química Orgánica, Facultad de Ciencias, Unidad de Excelencia de Química Aplicada a Biomedicina y Medioambiente (UEQ), Universidad de Granada (UGR)
Avda. Fuente Nueva S/N, 18071 Granada (Spain)

Dr. L. Đorđević, Prof. S. I. Stupp
Center for Bio-inspired Energy Science, Northwestern University
2145 Sheridan Road, Evanston, IL 60208 (USA)

Prof. R. M. Young, P. J. Brown, Prof. M. R. Wasielewski
Institute for Sustainability and Energy at Northwestern, Northwestern University
2145 Sheridan Road, Evanston, IL 60208 (USA)

Dr. H. Sai, Prof. S. I. Stupp
Simpson Querrey Institute for BioNanotechnology, Northwestern University
303 E. Superior Street, Chicago, IL 60611 (USA)
and
Department of Materials Science and Engineering, Northwestern University
2220 Campus Drive, Evanston, IL 60208 (USA)

Dr. L. Le Bras
Laboratoire Chrono-environnement (UMR 6249), Université de Bourgogne Franche-Comté
16 route de Gray, 25030 Besançon (France)

Dr. A. Perrier
Chimie Paris Tech, PSL Research University, CNRS, Institute of Chemistry for Life and Health Sciences (i-CLeHS), UMR 8060
75005 Paris (France)
and
Université Paris Cité
75006 Paris (France)

Prof. S. I. Stupp
Department of Biomedical Engineering, Northwestern University
2145 Sheridan Road, Evanston, IL 60208 (USA)
and
Department of Medicine, Northwestern University
676N St. Clair Street, Chicago, IL 60611 (USA)

Prof. J. F. Stoddart
School of Chemistry, University of New South Wales
Sydney, NSW 2052 (Australia)
and
Stoddart Institute of Molecular Science, Department of Chemistry, Zhejiang University
Hangzhou 310027 (China)
and
ZJU-Hangzhou Global Scientific and Technological Innovation Center
Hangzhou 311215 (China)

[+] These authors contributed equally to this work.

Introduction

Fluorophores exhibiting[1] aggregation-induced emission (AIE) are characterized by weak photoluminescence in solution and strong emission in the aggregated state. This photophysical phenomenon has found a wide range of applications from their association with organic light-emitting diodes[2] (OLEDs) to their use in theranostics[3] and bioimaging.[4] In addition, AIE addresses[5] the aggregation-caused quenching (ACQ) problem, which imposes limits on the performance of fluorophores in the solid state and condensed phases. While ACQ is the result of strong [π···π] stacking interactions in the aggregated state, AIE generally originates[6] from the restriction of the intramolecular motions (RIM) of fluorophores combining both vibrations and rotations. Thus, in the aggregated state, the degrees of freedom of the fluorophores are inhibited, leading to a significant increase in photoluminescence on account of favoring a radiative relaxation to the ground state instead of using non-radiative decay pathways, such as internal conversion (IC). In the past two decades, the majority of AIE-active fluorophores (AIEgens) described in the literature are based on silole[7] and tetraphenylethylene[8] (TPE) derivatives and have been used in the fabrication of smart optoelectronic materials. Tang et al.[9] have described various examples of these AIEgens which have been incorporated within organic optoelectronic devices. Recently, Yasuda et al.[10] have reported *o*-carborane-based fluorophores simultaneously possessing AIE and thermally activated delayed fluorescence. Furthermore, the development of novel AIEgens remains of intense interest. Increasing the library of fluorophores with wide optical windows for potential optoelectronic applications is a worthwhile pursuit.

Circularly polarized luminescence[11] (CPL) is a chiroptical property related to the difference between the left- and right-handed emissions of the circularly polarized light. CPL emission arises from photoluminescent non-racemic chiral species, i.e., small organic molecules,[12] organometallic complexes,[13] and materials.[14] The development of CPL emitters and acquisition techniques have led to some remarkable applications, such as sensors,[15] advanced security inks,[16] circularly polarized lasers[17] and organic light-emitting diodes.[18] In the context of small organic molecules, chiral cyclophanes have been shown recently to exhibit outstanding CPL responses, attaining[19] extremely high dissymmetry factor (g_{lum}) values. Chiral cyclophanes with CPL features have potential uses in the design and fabrication of chiral supramolecular assemblies and optoelectronic materials.

In recent times, the combination of CPL and AIE has become a focus of major interest[20] since, in the aggregated state, the CPL response can be enhanced and red-shifted while the handedness of the signal can be inverted. Although a plethora of chiral cyclophanes have been described,[21] rare examples have combined both CPL and AIE. In 2016, Zheng et al.[22] succeeded in the immobilization of the propeller-like conformation of TPE displaying AIE and CPL spectra in the aggregated state. In addition, Duan and Gong[23] reported a planar chiral boranyl-based [2.2]paracyclophane, which shows an amplified CPL emission upon aggregation.

During the past decade we have developed[24] a series of cationic cyclophanes by inserting planar aromatic moieties in between the two bipyridinium units of cyclobis(paraquat-*p*-phenylene) (**CBPQT^{4+}**). The photoluminescence properties of these compounds with rigid structures can be tuned depending on the nature of the incorporated moieties, e.g., anthracene[25] and thiazolothiazole,[26] exhibiting, respectively, yellowish-green and blue emissions. These tetracationic cyclophanes have been used as precursors in the synthesis of homo[2]catenanes, host–guest complexes for photon upconversion processes and probes for live-cell imaging on account of their high solubility in aqueous solutions. Even though we have previously developed[27] **CBPQT^{4+}**-based cyclophanes with enantiopure binaphthol bridges, CPL photoluminescence has not yet been investigated. In this context, the insertion of chiral moieties into the tetracationic cyclophane constitution should lead to CPL photoluminescence with attractive applications in sensing and biomedicine.

Binaphthyl is a well-known[28] axially chiral building block with a high racemization barrier and inherent photoluminescence properties. It has been shown previously to afford[29] AIEgens and CPL emitters. Herein, we designed and synthesized the enantiopure binaphthyl-based tetracationic cyclophanes, (*RR*)- and (*SS*)-**$^{6,6'}$BinBox**·4 PF_6, by inserting axially chiral binaphthyl moieties between two pyridinium units. The compounds and their precursors have been characterized by NMR spectroscopy, HR-MS and X-ray crystallographic techniques. Serendipitously, the cationic compounds have shown AIE which has been investigated by steady-state UV/Vis and fluorescence spectrophotometries as well as by transient absorption and fluorescence spectroscopies. The morphologies of aggregates have been characterized using atomic force, transmission electron, and confocal microscopies in addition to dynamic light scattering (DLS), while the chiroptical properties (electronic circular dichroism (ECD) and CPL) of the cationic compounds have been studied in their solution-phase and aggregated states. The origin of the AIE has been supported by molecular dynamics (MD) and quantum mechanical (QM) calculations.

Results and Discussion

Synthesis and characterization of (RR)- and (SS)-$^{6,6'}$BinBox·4 PF_6

The syntheses of the two enantiopure tetracationic cyclophanes (*RR*)- and (*SS*)-**$^{6,6'}$BinBox**·4 PF_6 are summarized in Scheme 1. The S_N2 reactions between (*R*)/(*S*)-**$^{6,6'}$BinBPy** and a large excess of α,α′-dibromo-*p*-xylene at 80 °C in a mixture of $MeCN/CH_2Cl_2$ afforded the corresponding dicationic benzyl bromides (*R*)/(*S*)-**$^{6,6'}$BinDB**·2 PF_6 in 67–71 % yields. The macrocyclization step was performed with (*R*)/(*S*)-**$^{6,6'}$BinDB**·2 PF_6 and (*R*)/(*S*)-**$^{6,6'}$BinBPy** using TBAI as catalyst, giving rise to the two enantiomerically pure, axially chiral cyclophanes (*RR*)- and (*SS*)-**$^{6,6'}$BinBox**·4 PF_6 in 14 and

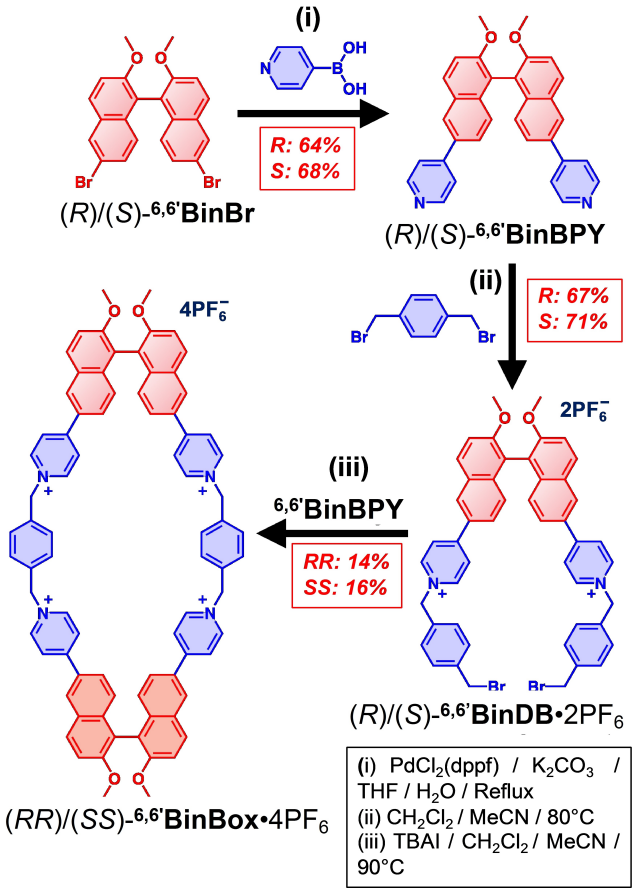

Scheme 1. Synthesis of the axially chiral binaphthyl-based cyclophanes (*RR*)/(*SS*)-$^{6,6'}$**BinBox**·4 PF_6.

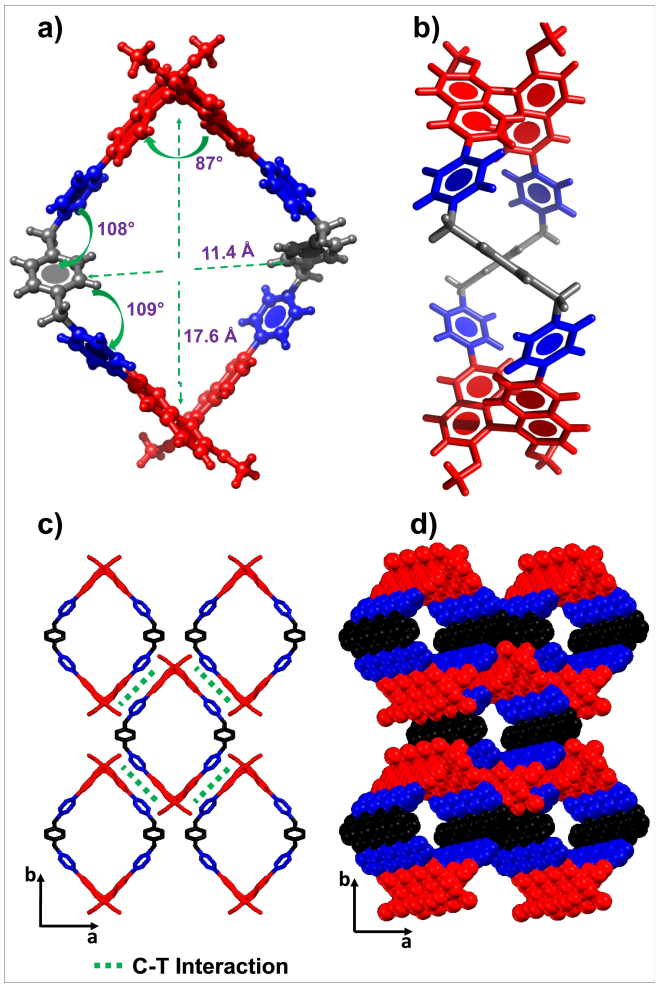

Figure 1. a) Top view and b) side-on view of the X-ray crystal structure of (*SS*)-$^{6,6'}$**BinBox**·4 PF_6 showing a square-like and a figure-eight-like structure, respectively. Along the *c*-axis, the packing of the solid-state structure of (*SS*)-$^{6,6'}$**BinBox**·4 PF_6 displays c) CT interactions between the pyridinium units and the binaphthyl moieties and exhibits d) a tubular superstructure.

16 % yields, respectively. For more details see the Supporting Information. A combination of NMR spectroscopies and high-resolution mass spectrometry confirmed (Figures S9–S12 and S15) the formation of cyclophanes (*RR*)/(*SS*)-$^{6,6'}$**BinBox**·4 PF_6.

Single-crystal X-ray diffraction analysis[30] (SC-XRD) provided (Figure 1) evidence for the formation of the enantiopure cyclophane (*SS*)-$^{6,6'}$**BinBox**$^{4+}$. Single crystals of (*SS*)-$^{6,6'}$**BinBox**$^{4+}$ were grown by slow vapor diffusion of $^{i}Pr_2O$ into a solution of (*SS*)-$^{6,6'}$**BinBox**·4 PF_6 in MeCN over a period of one week. (*SS*)-$^{6,6'}$**BinBox**$^{4+}$ crystallizes in the orthorhombic *C*222 space group revealing (Figure 1a) a square box-like structure in the solid state. The cavity of the cyclophane measures 17.6 Å between the two binaphthyl subunits and 11.4 Å between the two *para*-xylylene linkers. Remarkably, from the side-on view, the solid-state structure reveals (Figure 1b) a figure-eight geometry leading to an additional helicity in the cyclophane manifested on the bridge between the two axially chiral binaphthyl moieties. The packing of the (*SS*)-$^{6,6'}$**BinBox**$^{4+}$, along the *c*-axis, reveals (Figures 1c,d) a unique rhombic and tubular superstructure on account of the head-to-tail, donor–acceptor charge transfer (CT) interactions.

Steady-state optical properties

The steady-state absorption and fluorescence of the compounds (*R*)/(*S*)-$^{6,6'}$**BinBPy**, (*R*)/(*S*)-$^{6,6'}$**BinDB**·2 PF_6 and (*RR*)/(*SS*)-$^{6,6'}$**BinBox**·4 PF_6 have been investigated. While (*R*)/(*S*)-$^{6,6'}$**BinBPy** displays (Figure 2 and S18) absorption bands between 268 and 370 nm in DMF ($\varepsilon = 5.9 \times 10^4\ M^{-1}cm^{-1}$ at 271 nm), the two pyridinium-containing compounds, (*R*)/(*S*)-$^{6,6'}$**BinDB**·2 PF_6 and (*RR*)/(*SS*)-$^{6,6'}$**BinBox**·4 PF_6, exhibit (Figures 2, S19 and S20) additional bands between 325 nm and 450 nm ($\varepsilon = 3.5 \times 10^4$ and $5.2 \times 10^4\ M^{-1}cm^{-1}$ at 385 and 386 nm for (*R*)/(*S*)-$^{6,6'}$**BinDB**·2 PF_6 and (*RR*)/(*SS*)-$^{6,6'}$**BinBox**·4 PF_6, respectively) originating from intramolecular CT between the binaphthyl moieties and the pyridinium units. The compounds (*R*)/(*S*)-$^{6,6'}$**BinBPy** display (Figure S18) an intense blue emission in DMF centered on 395 nm (quantum yields (Φ_F) = 19 %), while (*R*)/(*S*)-$^{6,6'}$**BinDB**·2 PF_6 and (*RR*)/(*SS*)-$^{6,6'}$**BinBox**·4 PF_6 emit (Figures S19–S20) a yellowish-

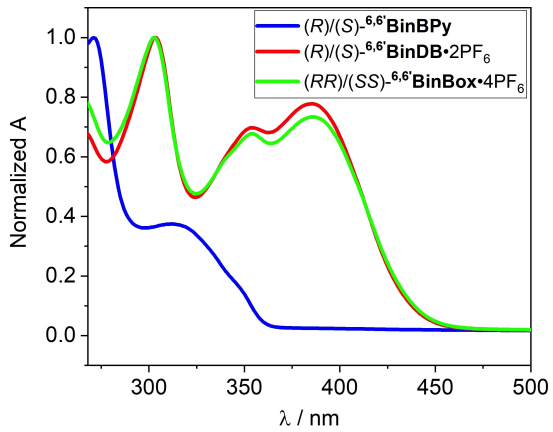

Figure 2. Steady-state absorption spectra of (*R*)/(*S*)-**6,6′BinBPy**, (*R*)/(*S*)-**6,6′BinDB**·2 PF_6 and (*RR*)/(*SS*)-**6,6′BinBox**·4 PF_6.

green fluorescence between 450 and 700 nm with peaks at 532 nm ($\Phi_F = 0.61\,\%$) and 537 nm ($\Phi_F = 0.56\,\%$), respectively. This red-shifting of fluorescence in these cationic compounds is a result[25] of their intramolecular CT character.

The calculated photophysical properties (Tables S5–S7, Figures S80–S83 and S87–S88) are in complete agreement with the experimental results. Intramolecular CT was present (Figure 3) in all three compounds, i.e., (*S*)-**6,6′BinBPy**, (*S*)-**6,6′BinDB^{2+}**, (*SS*)-**6,6′BinBox^{4+}**, arising from electron transfer from the binaphthyl moieties to the pyridine/pyridinium units. This CT is more pronounced for one of the cationic species (*S*)-**6,6′BinDB^{2+}**, as illustrated by the large values for the amount of charge transferred q_{CT} (0.822 and 0.850 e), the CT distance d_{CT} (2.783 and 2.761 Å), and the CT dipole moment $|\mu_{CT}|$ (10.9 and 10.7 D) for both $S_0 \rightarrow S_1$ and $S_0 \rightarrow S_2$ transitions. In the case of the cyclophane (*SS*)-**6,6′BinBox^{4+}** the symmetrical structure leads to a global compensation of the CT around the two binaphthyl moieties, giving rise to smaller d_{CT} and $|\mu_{CT}|$ values, but similar q_{CT} values.

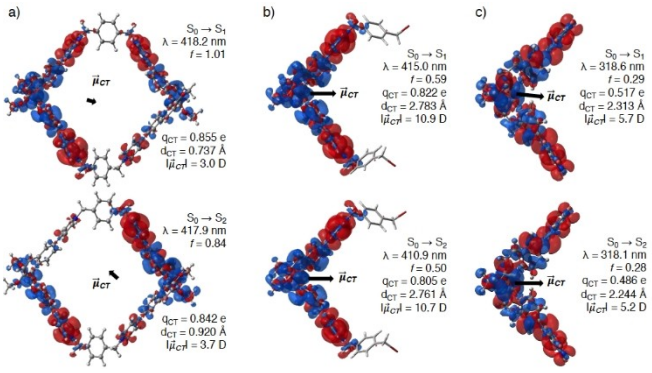

Figure 3. Representation of the electron density difference (EDD, $\Delta\rho(r)$) for the first two main electronic transitions, $S_0 \rightarrow S_1$ (top) and $S_0 \rightarrow S_2$ (bottom), respectively, for a) (*SS*)-**6,6′BinBox^{4+}**, b) (*S*)-**6,6′BinDB^{2+}**, and c) (*S*)-**6,6′BinBPy**. The gain (or loss) of electronic density is represented in red (or blue). For each transition, the amount of transferred charge (q_{CT}), the distance of CT (d_{CT}) and the norm of the CT dipole moment ($|\vec{\mu}_{CT}|$) have also been provided along with the corresponding calculated absorption wavelength (λ) and oscillator strength (*f*).

During the synthesis of the cyclophane (*RR*)/(*SS*)-**6,6′BinBox**·4 PF_6 a bright yellowish-green emission was observed by the naked eye upon precipitation. This observation encouraged us to investigate the photoluminescence of aggregates of all the compounds. In order to explore the possibility of AIE, the H_2O fraction (f_w) of the DMF solutions of (*R*)/(*S*)-**6,6′BinBPy**, (*R*)/(*S*)-**6,6′BinDB**·2 PF_6 and (*RR*)/(*SS*)-**6,6′BinBox**·4 PF_6 was gradually increased from 0 to 90 %, triggering the formation of aggregates and leading to (Figure 4) turbid suspensions. For the neutral (*R*)/(*S*)-**6,6′BinBPy** precursor, upon aggregation, the fluorescence intensity decreased (Figures S23–S24), initially, then increased (after $f_w = 70\,\%$) but never reached its original value. Conversely, in the case of the cationic compounds, i.e., (*R*)/(*S*)-**6,6′BinDB**·2 PF_6 and (*RR*)/(*SS*)-**6,6′BinBox**·4 PF_6, the addition of H_2O into the DMF solutions and the formation of aggregates gave rise to a significant increase of the photoluminescence intensity (Figure 4), accompanied by a weak hypsochromic shift of 7 nm. In addition, an increase of fluorescence Φ_F from 0.61 to 5.7 % for (*R*)/(*S*)-**6,6′BinDB**·2 PF_6 and from 0.56 to 2.2 % for (*RR*)/(*SS*)-**6,6′BinBox**·4 PF_6 was detected upon aggregation, an observation which is in complete agreement with the presence of AIE. A similar phenomenon was observed

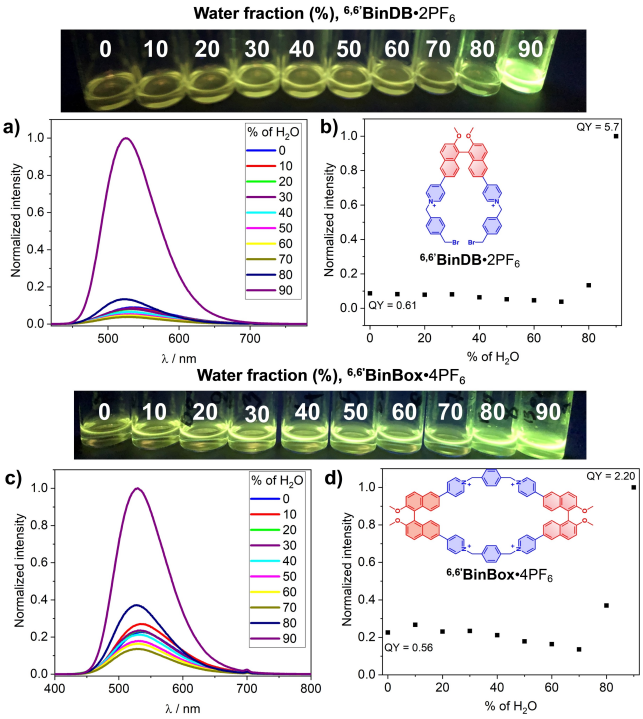

Figure 4. AIE Investigation on the cyclophanes (*RR*)/(*SS*)-**6,6′BinBox**·4 PF_6 and compounds (*R*)/(*S*)-**6,6′BinDB**·2 PF_6 in different mixtures of DMF/H_2O. Emission spectra ($\lambda_{exc} = 350$ nm) of a) (*R*)/(*S*)-**6,6′BinDB**·2 PF_6 and (c) (*RR*)/(*SS*)-**6,6′BinBox**·4 PF_6, and the normalized intensity of the emission spectra of b) (*R*)/(*S*)-**6,6′BinDB**·2 PF_6 and d) (*RR*)/(*SS*)-**6,6′BinBox**·4 PF_6 at λ = 529 nm in those different solvent mixtures versus the percentage of H_2O.

(Figures S29–S32) in mixtures of MeCN/H_2O. UV/Vis spectroscopy was carried out in (Figures S33–S35) DMF/H_2O mixtures. Upon addition of H_2O, no major changes were detected compared to the pure DMF solutions, except for a slight broadening of the absorption bands which we attributed to the turbidity of the suspension. The photoluminescence results prove clearly that the pyridinium-containing binaphthyl-based compounds, i.e., (*R*)/(*S*)-**$^{6,6'}$BinDB**·2 PF_6 and (*RR*)/(*SS*)-**$^{6,6'}$BinBox**·4 PF_6, exhibit AIE in contrast with the neutral pyridine-containing binaphthyl (*R*)/(*S*)-**$^{6,6'}$BinBPy** which shows ACQ.

Morphologies of the aggregates

The morphologies of the (*R*)/(*S*)-**$^{6,6'}$BinDB**·2 PF_6 and (*RR*)/(*SS*)-**$^{6,6'}$BinBox**·4 PF_6 aggregates formed in 90:10 H_2O/DMF were imaged (Figures 5a–f) by atomic force microscopy (AFM), transmission electron microscopy (TEM) and confocal laser-scanning microscopy (CLSM). Drop-casted samples on mica showed (Figure 5a,b and Figure S76) the presence of spherical nanoparticles with sizes ranging from 5 to 110 nm as indicated by AFM. They were also observed (Figure 5c,d) by negative-stained TEM. Since the aggregates exhibit AIE, we also used CLSM to confirm the presence of fluorescent nanoparticles (Figure 5e,f) and extracted their fluorescence spectra (Figure 5g), which showed (Figure 4) the same emission profiles as those observed by steady-state fluorescence. In an attempt to complement the microscopic characterizations, we also carried out DLS on (*R*)/(*S*)-**$^{6,6'}$BinDB**·2 PF_6 and (*RR*)/(*SS*)-**$^{6,6'}$BinBox**·4 PF_6 DMF/H_2O (1:9) samples, confirming the presence of spherical nanoparticles in solution with a broad range of sizes comparable to those observed by microscopic techniques. Figure 5 presents results for (*R*)-**$^{6,6'}$BinDB**·2 PF_6 and (*RR*)-**$^{6,6'}$BinBox**·4 PF_6, while their enantiomers, which showed similar morphologies, are to be found in the Supporting Information (Figures S75 and S77).

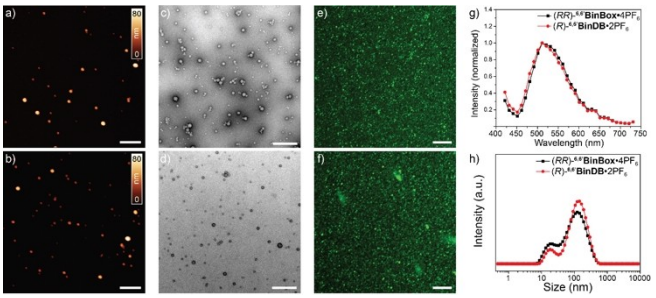

Figure 5. Morphological characterization of the aggregates of (*R*)-**$^{6,6'}$BinDB**·2 PF_6 and (*RR*)- **$^{6,6'}$BinBox**·4 PF_6 formed in 90:10 H_2O/DMF. a,b) AFM of drop-casted samples on mica of a) (*R*)-**$^{6,6'}$BinDB**·2 PF_6 and b) (*RR*)- **$^{6,6'}$BinBox**·4 PF_6. Scale bars are 500 nm. c,d) TEM of negatively-stained samples of c) (*R*)-**$^{6,6'}$BinDB**·2 PF_6 and d) (*RR*)-**$^{6,6'}$BinBox**·4 PF_6. Scale bars are 500 nm. e,f) CLSM of liquid samples of a) (*R*)-**$^{6,6'}$BinDB**·2 PF_6 and b) (*RR*)-**$^{6,6'}$BinBox**·4 PF_6. Scale bars are 10 μm. g) Extracted emission spectra from confocal-laser scanning experiments. h) DLS of aggregates.

Investigation of the AIE mechanism

QM calculations and MD simulations. An efficient combination[31] of QM calculations and MD simulations was adopted to investigate the origin of the AIE. The detailed protocols are presented in the Supporting Information.

The aggregation process for all three compounds, i.e., (*S*)-**$^{6,6'}$BinBPy**, (*S*)-**$^{6,6'}$BinDB^{2+}**, (*SS*)-**$^{6,6'}$BinBox^{4+}**, was investigated employing MD simulations, starting from four independent and distant molecules. The formation of small oligomers has been observed (Figure 6 and Figure S79) systematically for all compounds showing a dimer for (*SS*)-**$^{6,6'}$BinBox^{4+}**, a tetramer for (*S*)-**$^{6,6'}$BinDB^{2+}** and a trimer for (*S*)-**$^{6,6'}$BinBPy**. Neutral (*S*)-**$^{6,6'}$BinBPy** molecules reveal (Figure 6c) a perfectly stacked and interwoven trimer characterized by [π···π] interactions. These specific interactions, obtained from a noncovalent interactions (NCI) plot analysis, are only found in the case of (*S*)-**$^{6,6'}$BinBPy** oligomers. Oligomers of the three compounds are stabilized (Figure 6) by [C–H–π] interactions, either between donor-donor, acceptor-acceptor or donor-acceptor parts of the different molecules.

Additional calculations were performed on the vibrational motion and electronic energy transfer. The weak emissive behavior of the three compounds in DMF can be attributed (Figures S90–S91) to torsional vibrational motions around the axes of chirality associated with the binaphthyl moieties which play a critical role in the non-radiative deexcitation pathway. In the aggregated state, these vibrations become limited, and an increase of Φ_F is anticipated in

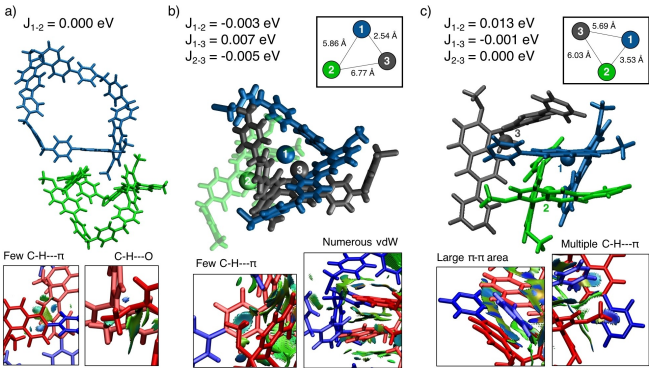

Figure 6. Representation of the oligomers that were obtained after a 50-ns long MD simulation involving four molecules for a) (*SS*)-**$^{6,6'}$BinBox^{4+}**, b) (*S*)-**$^{6,6'}$BinDB^{2+}**, and c) (*S*)-**$^{6,6'}$BinBPy**. For simplicity, each of these structures is represented in a different color (blue, green and gray). For (*S*)-**$^{6,6'}$BinDB^{2+}** and (*S*)-**$^{6,6'}$BinBPy**, the center of mass (COM) of each cyclophane is shown as a large colored dot,and a schematic representation of the COMs and the distance between them is provided. The calculated electronic energy transfer, also known as excitonic coupling, J_{i-j}, between each pair of molecules is also given. The main noncovalent interactions ([C–H–π], van der Waals, and [π···π]) for each oligomer are depicted as isosurfaces ($s(r) = 0.4$) obtained via NCIplot. Attractive ([C–H–π] and [π···π]), repulsive (steric hindrance) and van der Waals interactions are represented in blue, red, and green respectively. The structures of (*SS*)-**$^{6,6'}$BinBox^{4+}**, (*S*)-**$^{6,6'}$BinDB^{2+}**, and (*S*)-**$^{6,6'}$BinBPy** have been represented in blue and red to visualize donor and acceptor areas of the molecules.

the case of all compounds. Remarkably, this behavior has been observed (Figure 4 and Table S3) experimentally only in the case of the cationic compounds, i.e., (*SS*)-**6,6′BinBox**$^{4+}$, and (*S*)-**6,6′BinDB**$^{2+}$, but not for the neutral (*S*)-**6,6′BinBPy**.

The calculated electronic energy transfer for the excitonic coupling $J_{i\text{-}j}$ between two molecules i and j in a dimer in the case of (*SS*)-**6,6′BinBox**$^{4+}$, (*S*)-**6,6′BinDB**$^{2+}$ is always lower than 0.007 eV, contrary to (*S*)-**6,6′BinBPy** ($J_{1\text{-}2}$ = 0.013 eV) which reveals (Figure 6c) that a new deexcitation pathway is possible. These calculations demonstrate that AIE for both cationic species arises from a RIM mechanism. Conversely, a subtle competition between RIM and excitation energy transfers in the neutral (*S*)-**6,6′BinBPy** inhibiting AIE and giving place to ACQ.

Excited-state dynamics. The excited-state dynamics of (*R*)/(*S*)-**6,6′BinDB**$^{2+}$ and (*RR*)/(*SS*)-**6,6′BinBox**$^{4+}$ were explored using transient absorption (TA) and time-resolved fluorescence (TRF) spectroscopies. Following excitation of (*R*)/(*S*)-**6,6′BinDB**$^{2+}$ in DMF at 440 nm, we observed rapid population of the intramolecular charge transfer (ICT) state in less than 300 fs, (Figure S38) showing a ground-state bleach with a minimum at 392 nm and excited-state absorption (ESA) with maxima at 333, 446, and 700 nm. Importantly, we also observed a stimulated emission (SE) feature at 530 nm, which correlates well with the steady-state emission and is assigned as radiative CT recombination (k_{CR1}, Figure 4a). This feature ostensibly vanishes, along with shifting of the 446 nm ESA features to 421 nm. The 700-nm feature loses definition, while a new shoulder appears at 547 nm as the ICT state relaxes. The decay of this state occurs with a rate constant of $k_1 = k_{CR1} + k_{relax} = (4.9 \pm 0.3\ \text{ps})^{-1}$, which includes contributions from relaxation and radiative recombination of the ICT state. The relaxed ICT state undergoes integer charge separation (CS), wherein the binaphthyl moiety is fully oxidized and one of the neighboring pyridinium groups is fully reduced, possibly as a consequence of the interactions shown in Figure 6c. The CS state forms with a rate constant of $k_2 = k_{CR2} + k_{CS} = (860 \pm 20\ \text{ps})^{-1}$, and then decays by charge recombination to the ground state (k_{CR3}) and the local triplet state ($k_{CR\text{-}T}$): $k_3 = k_{CR3} + k_{CR\text{-}T} = (1.5 \pm 0.6\ \text{ns})^{-1}$. While there is no fully negative SE feature in the TA spectrum of the CS state, the TRF data (Figures S46–S49) suggest that the local minimum at 595 nm is due to a negative SE atop a broad, positive ESA, and that this state can radiatively recombine to give the weak emission that decays with that lifetime. The small Φ_F values (Figure 4b) are consistent with the rapid deactivation of the initial emissive state. The longer-lived product states, however, also contribute to the overall emission, albeit weakly. In 90:10 H_2O/DMF, the same features are observed for (*R*)/(*S*)-**6,6′BinDB**$^{2+}$ and the relaxation of the initial ICT state becomes biexponential (Figures S40–S41 and Table S4).

The dynamics of (*RR*)/(*SS*)-**6,6′BinBox**$^{4+}$ in DMF are similar following 440-nm excitation (Figures S42–S43). The CT-excited state SE minimum red-shifts from 524 to 556 nm with $k_1 = (2.1 \pm 0.3\ \text{ps})^{-1}$ before forming the local (positive) minimum at 595 nm with $k_{1'} = (6.5 \pm 0.8\ \text{ps})^{-1}$. While aggregation is not expected without the addition of water, the biphasic decay of the emissive state suggests that in order to accommodate the excited-state charge distribution, the cyclophane has to undergo structural relaxation, i.e., not accessible in the corresponding (*R*)/(*S*)-**6,6′BinDB**$^{2+}$ system. CS quenches the emission with $k_2 = (860 \pm 10\ \text{ps})^{-1}$, then recombination occurs with $k_3 = (2.8 \pm 0.6\ \text{ns})^{-1}$ (Figures S36–S37). Again, the TRF spectra show long-lived emissive components.

Figure 7 shows the dynamics of aggregates of (*RR*)/(*SS*)-**6,6′BinBox**$^{4+}$ in 90:10 H_2O/DMF upon 440-nm excitation (Figure S44–S45). ESA features at 358, 439 and 662 nm, along with bleaching at 389 nm and SE at 532 nm. These features all decay with $k_1 = (3.6 \pm 0.3\ \text{ps})^{-1}$ (Figures S38–S39). CS similarly occurs with $k_2 = (1.01 \pm 0.03\ \text{ns})^{-1}$, while recombination occurs with $k_3 \approx (3\text{–}5\ \text{ns})^{-1}$.

The excited-state dynamics are summarized in Figure 7d. The RIM or distortion of the cyclophane's geometry upon aggregation slows the relaxation of the CT-excited state. Besides this, however, aggregation does not appear to have any measurable impact on the excited-state lifetimes. Since the observed rate constants are the sum of those of the radiative (recombination) and non-radiative pathways, the dramatic increase in Φ_F upon aggregation (Figure 4d) suggests that the values of the recombination constants are increasing while those of the non-radiative constants are lowered ($\Phi_f = k_{rad}/k_{total}$). Such an effect by RIM has been demonstrated previously, as these rates are highly sensitive to instantaneous changes in the energy levels induced[32] by fluctuations of the molecule and its environment.

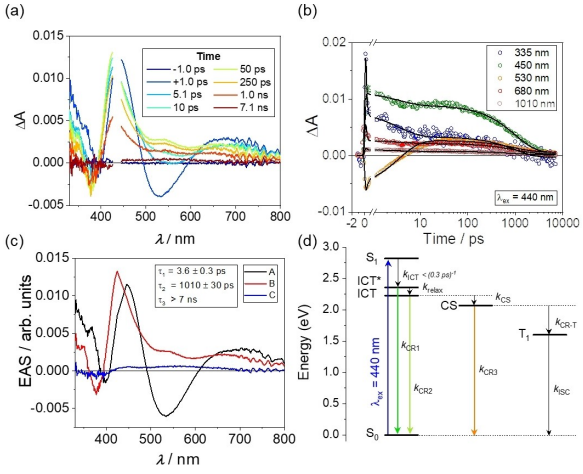

Figure 7. Transient absorption (TA) data for **6,6′BinBox**·4 PF_6 in a H_2O/DMF (90:10) mixture excited at 440 nm. a) Spectra at selected time delays. b) Kinetic Fits. c) Evolution-associated spectra after photoexcitation and time constants d) State diagram showing competitive decay pathways: intramolecular charge transfer (ICT), structural/vibrational relaxation (relax), radiative charge recombination (CR1, CR2, and CR3), charge separation (CS), charge recombination to the triplet state (CR-T), and intersystem crossing (ISC). Aggregation causes relaxation to decay biexponentially.

Chiroptical properties

The axially chiral compounds displaying AIE, i.e., (*R*)/(*S*)-**6,6′BinDB**·2 PF_6 and (*RR*)/(*SS*)-**6,6′BinBox**·4 PF_6, were also investigated by ECD and CPL spectroscopies. ECD spectra of cyclophanes (*RR*)/(*SS*)-**6,6′BinBox**·4 PF_6 and compounds (*R*)/(*S*)-**6,6′BinDB**·2 PF_6, display (Figure 8a,c) mirror images for both enantiomers with alternate Cotton effects from 280 to 450 nm in DMF. With respect to the lowest energy transition, (*S*)-**6,6′BinDB**·2 PF_6 exhibits a positive Cotton effect at 401 nm ($|\Delta\varepsilon| \approx 16\ M^{-1}cm^{-1}$, $g_{abs} = \Delta\varepsilon/\varepsilon \approx 6.0\times10^{-4}$) and (*SS*)-**6,6′BinBox**·4 PF_6 displays a much stronger positive Cotton effect at 403 nm ($|\Delta\varepsilon| \approx 80\ M^{-1}cm^{-1}$, $g_{abs} \approx 1.8\times10^{-3}$). Furthermore, the theoretical (Figure S84) and the experimental ECD spectra of these two sets of enantiomers are in good agreement for **6,6′BinDB^{2+}**. For (RR)- and (SS)-**6,6′BinBox^{4+}**, the red shift of the calculated excitation energies compared to experiment (Figure S88) leads to a less efficient but convincing agreement between the calculated and experimental ECD spectra (Figure S89).

Upon excitation with UV light ($\lambda_{exc} = 395$ nm), CPL spectra were recorded from 450 to 700 nm. Although the enantiomers of compounds (*R*)/(*S*)-**6,6′BinDB**·2 PF_6 and cyclophanes (*RR*)/(*SS*)-**6,6′BinBox**·4 PF_6 exhibit (Figure 8b,d) mirror image CPL responses, indicating a true CPL signal,[11a] both compounds afford very distinct luminescence dissymmetry factors ($|g_{lum}|$), calculated as $g_{lum} = 2(I^L - I^R)/(I^L + I^R)$, where I^L and I^R correspond to the intensities of left- and right-handed circularly polarized light emitted by the chiral luminophores. The compound (*S*)-**6,6′BinDB**·2 PF_6 yields (Figure S57) a positive g_{lum} value of $+2.0\times10^{-4}$, while the cyclophane (*SS*)-**6,6′BinBox**·4 PF_6 gives (Figure S61) a much stronger positive g_{lum} value of $+0.8\times10^{-3}$.[33] Similar ECD and CPL spectra have been obtained (Figures S62–S69) for both (*R*)/(*S*)-**6,6′BinDB**·2 PF_6 and (*RR*)/(*SS*)-**6,6′BinBox**·4 PF_6 in MeCN.

Having fully characterized the AIE and the chiroptical properties of (*RR*)/(*SS*)-**6,6′BinBox**·4 PF_6 and (*R*)/(*S*)-**6,6′BinDB**·2 PF_6 in solution we evaluated the CPL responses of the aggregates from these two sets of enantiomers in a mixture of DMF/H_2O (1:9). The CPL spectra recorded for (*RR*)/(*SS*)-**6,6′BinBox**·4 PF_6 (Figure 8e–f) and (*R*)/(*S*)-**6,6′BinDB**·2 PF_6 (Figure S70) exhibit signals of the same handedness as those recorded in solution. The absolute values of the intensities for the signals from (*R*)-**6,6′BinDB**·2 PF_6 and (*RR*)-**6,6′BinBox**·4 PF_6 are higher than those of the corresponding enantiomeric forms. The CPL signals[34] of the enantiomers of each compound are of opposite signs, which proves the existence of a contribution that corresponds to CPL. The signals are, however, contaminated with a linear polarization (LP) component of negative intensity even though the CPL measurements were performed using a 180° measuring configuration with unpolarized exciting light which renders the photoselection phenomenon negligible and minimizes the LP effects.[35] This LP component is a result of the formation of aggregated species that might adopt a preferential orientation in the solvent media giving rise to anisotropy. As a result, the CPL signals of the enantiomers are not mirror images, a situation which has also been reported[36] previously in some aggregates or solid-state systems. The $|g_{lum}|$ values of the aggregates can be, therefore, estimated to be *ca.* 1.2×10^{-3} for (*RR*)/(*SS*)-**6,6′BinBox**·4 PF_6 and *ca.* 3.3×10^{-4} for (*R*)/(*S*)-**6,6′BinDB**·2 PF_6.

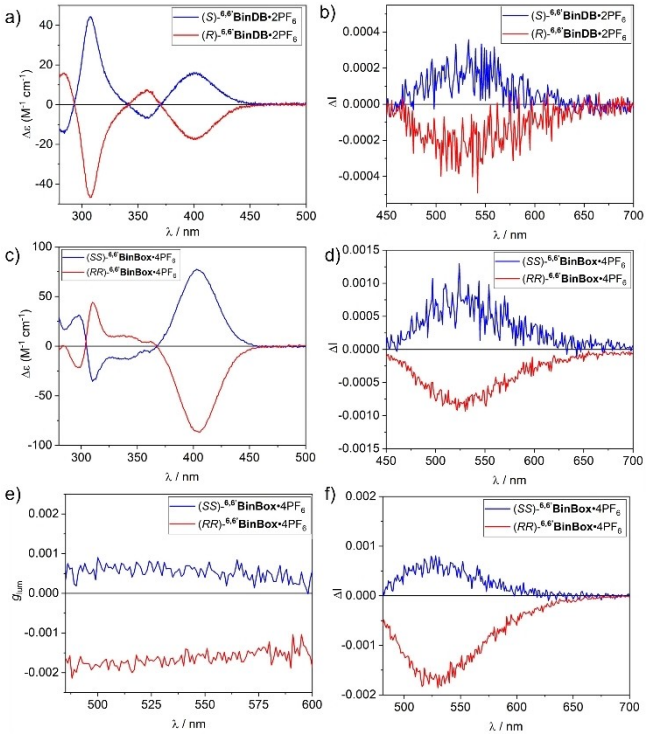

Figure 8. Chiroptical properties of the axially chiral binaphthyl-containing (*R*)/(*S*)-**6,6′BinDB**·2 PF_6 and (*RR*)/(*SS*)-**6,6′BinBox**·4 PF_6. a) ECD and b) CPL ($\lambda_{exc} = 395$ nm) spectra of compound (*R*)/(*S*)-**6,6′BinDB**·2 PF_6 in DMF. c) ECD and d) CPL ($\lambda_{exc} = 395$ nm) spectra of compound (*RR*)/(*SS*)-**6,6′BinBox**·4 PF_6 in DMF. e) g_{lum} and f) CPL spectra ($\lambda_{exc} = 435$ nm) for the aggregates of (*RR*)/(*SS*)-**6,6′BinBox**·4 PF6 in a mixture of DMF/H_2O (1:9).

Conclusion

In summary, two enantiopure binaphthyl-based tetracationic cyclophanes have been synthesized by insertion of axially chiral binaphthyl moieties between the pyridinium units. Single-crystal X-ray diffraction analysis of the enantiopure cyclophanes showed a unique figure-eight and square-like geometry. These fluorescent cyclophanes exhibit aggregation-induced emission behavior leading to a significant enhancement of their quantum yields. Spherical nanoparticle morphologies have been observed for the aggregates. Theoretical calculations have demonstrated that the aggregation-induced emission originates from the restriction of torsional motions around the axes of chirality associated with the binaphthyl moieties upon aggregation. Data from time-resolved absorption and fluorescence spectroscopies suggest that a change in the global structure of the cyclophanes upon aggregation fine-tunes the electronic coupling and the excited state dynamics, leading to an increase of the

fluorescence quantum yields. In addition, these axially chiral tetracationic cyclophanes afford efficient circularly polarized luminescence performances, both in solution and in the aggregated states. The duality of aggregation-induced emission and circularly polarized luminescence properties render these cyclophanes potential candidates for future applications in biomedicine and the fabrication of photonic devices.

Acknowledgements

The authors thank Northwestern University for their continued support of this research, the National Science Foundation under grant number DMR-2003739 (M.R.W.), the Center for Bio-Inspired Energy Science (CBES), an Energy Frontier Research Center funded by the U.S. Department of Energy, under Award No. DE-SC0000989 (S.I.S.). This work made use of the EPIC (TEM) and Keck-II (DLS) facilities of Northwestern University's NUANCE Center, which has received support from the SHyNE Resource (NSF ECCS-2025633), the IIN, and Northwestern's MRSEC program (NSF DMR-1720139. M.D.C, A.G.C. and V.B. thank the financial support given by grants EQC2019-006543-P, funded by MCIN/AIE/10.13039/501100011033 and "ERDF A way of making Europe", and P18-FR-2877, funded by FEDER(ERDF)/Junta de Andalucía-Consejería de Transformación Económica, Industria, Conocimiento y Universidades. L.L.B would like to thank the supercomputer facilities of the Mésocentre de calcul de Franche-Comté. A.P. would like to thank CINES and IDRIS for the access to the HPC resources (allocations 2021 and 2022-A0010810135) made by GENCI.

Conflict of Interest

The authors declare no conflict of interest.

Data Availability Statement

The data that support the findings of this study are available in the supplementary material of this article.

Keywords: Aggregation-Induced Emission · Chirality · Circularly Polarized Luminescence · Macrocycles · Optoelectronics

[1] a) J. Z. Luo, Z. Xie, J. W. Y. Lam, L. Cheng, H. Chen, C. Qiu, H. S. Kwok, X. Zhan, Y. Liu, D. Zhu, B. Z. Tang, *Chem. Commun.* **2001**, 1740–1741; b) J. Mei, N. L. C. Leung, R. T. K. Kwok, J. W. Y. Lam, B. Z. Tang, *Chem. Rev.* **2015**, *115*, 11718–11940; c) Y. Wang, J. Nie, W. Fang, L. Yang, Q. Hu, Z. Wang, J. Z. Sun, B. Z. Tang, *Chem. Rev.* **2020**, *120*, 4534–4577; d) Y. Tang, B. Z. Tang, *Handbook of Aggregation-Induced Emission*, Wiley, Hoboken, **2022**.

[2] a) W. Qin, J. W. Y. Lam, Z. Yang, S. Chen, G. Liang, W. Zhao, H. S. Kwok, B. Z. Tang, *Chem. Commun.* **2015**, *51*, 7321–7324; b) J. Guo, X.-L. Li, H. Nie, W. Luo, S. Gan, S. Hu, R. Hu, A. Qin, Z. Zhao, S.-J. Su, B. Z. Tang, *Adv. Funct. Mater.* **2017**, *27*, 1606458; c) Y. Li, Z. Xu, X. Zhu, B. Chen, Z. Wang, B. Xiao, J. W. Y. Lam, Z. Zhao, D. Ma, B. Z. Tang, *ACS Appl. Mater. Interfaces* **2019**, *11*, 17592–17601.

[3] a) G. Feng, B. Liu, *Acc. Chem. Res.* **2018**, *51*, 1404–1414; b) J. Huang, B. He, Z. Zhang, Y. Li, M. Kang, Y. Wang, K. Li, D. Wang, B. Z. Tang, *Adv. Mater.* **2020**, *32*, 2003382; c) Z. Zhang, M. Kang, H. Tan, N. Song, M. Li, P. Xiao, D. Yan, L. Zhang, D. Wang, B. Z. Tang, *Chem. Soc. Rev.* **2022**, *51*, 1983–2030.

[4] a) H. Lu, Y. Zheng, X. Zhao, L. Wang, S. Ma, X. Han, B. Xu, W. Tian, H. Gao, *Angew. Chem. Int. Ed.* **2016**, *55*, 155–159; *Angew. Chem.* **2016**, *128*, 163–167; b) J. Lin, X. Zeng, Y. Xiao, L. Tang, J. Nong, Y. Liu, H. Zhou, B. Ding, F. Xu, H. Tong, Z. Deng, X. Hong, *Chem. Sci.* **2019**, *10*, 1219–1226; c) G. Niu, X. Zheng, Z. Zhao, H. Zhang, J. Wang, X. He, Y. Chen, X. Shi, C. Ma, R. T. K. Kwok, J. W. Y. Lam, H. H. Y. Sung, I. D. Williams, K. S. Wong, P. Wang, B. Z. Tang, *J. Am. Chem. Soc.* **2019**, *141*, 15111–15120.

[5] a) L. Zong, Y. Xie, C. Wang, J.-R. Li, Q. Li, Z. Li, *Chem. Commun.* **2016**, *52*, 11496–11499; b) Y. Li, S. Liu, H. Ni, H. Zhang, H. Zhang, C. Chuah, C. Ma, K. S. Wong, J. W. Y. Lam, R. T. K. Kwok, J. Qian, X. Lu, B. Z. Tang, *Angew. Chem. Int. Ed.* **2020**, *59*, 12822–12826; *Angew. Chem.* **2020**, *132*, 12922–12926.

[6] a) Y. Hong, J. W. Y. Lam, B. Z. Tang, *Chem. Commun.* **2009**, 4332–4353; b) F. Würthner, *Angew. Chem. Int. Ed.* **2020**, *59*, 14192–14196; *Angew. Chem.* **2020**, *132*, 14296–14301.

[7] a) Z. Zhao, B. He, B. Z. Tang, *Chem. Sci.* **2015**, *6*, 5347–5365; b) G. Lyu, T. J. F. Southern, B. L. Charles, M. Roger, P. Gerbier, S. Clément, R. C. Evans, *J. Mater. Chem. C* **2021**, *9*, 13914–13925.

[8] a) N. B. Shustova, B. D. McCarthy, M. Dincă, *J. Am. Chem. Soc.* **2011**, *133*, 20126–20129; b) D. D. La, S. V. Bhosale, L. A. Jones, S. V. Bhosale, *ACS Appl. Mater. Interfaces* **2018**, *10*, 12189–12216; c) H.-T. Feng, Y.-X. Yuan, J.-B. Xiong, Y.-S. Zheng, B. Z. Tang, *Chem. Soc. Rev.* **2018**, *47*, 7452–7476; d) J. Kaur, D. N. Nadimetla, S. V. Bhosale, P. K. Singh, *J. Phys. Chem. B* **2022**, *126*, 1147–1155.

[9] a) W. Z. Yuan, Y. Gong, S. Chen, X. Y. Shen, J. W. Y. Lam, P. Lu, Y. Lu, Z. Wang, R. Hu, N. Xie, H. S. Kwok, Y. Zhang, J. Z. Sun, B. Z. Tang, *Chem. Mater.* **2012**, *24*, 1518–1528; b) B. Liu, H. Nie, X. Zhou, S. Hu, D. Luo, D. Gao, J. Zou, M. Xu, L. Wang, Z. Zhao, A. Qin, J. Peng, H. Ning, Y. Cao, B. Z. Tang, *Adv. Funct. Mater.* **2016**, *26*, 776–783; c) Z. Zhao, H. Nie, C. Ge, Y. Cai, Y. Xiong, J. Qi, W. Wu, R. T. K. Kwok, X. Gao, A. Qin, J. W. Y. Lam, B. Z. Tang, *Adv. Sci.* **2017**, *4*, 1700005; d) J. Huang, H. Nie, J. Zeng, Z. Zhuang, S. Gan, Y. Cai, J. Guo, S.-J. Su, Z. Zhao, B. Z. Tang, *Angew. Chem. Int. Ed.* **2017**, *56*, 12971–12976; *Angew. Chem.* **2017**, *129*, 13151–13156.

[10] R. Furue, T. Nishimoto, I. S. Park, J. Lee, T. Yasuda, *Angew. Chem. Int. Ed.* **2016**, *55*, 7171–7175; *Angew. Chem.* **2016**, *128*, 7287–7291.

[11] a) J. P. Riehl, F. S. Richardson, *Chem. Rev.* **1986**, *86*, 1–16; b) G. Longhi, E. Castiglioni, J. Koshoubu, G. Mazzeo, S. Abbate, *Chirality* **2016**, *28*, 696–707.

[12] T. Mori, *Circularly Polarized Luminescence of Isolated Small Organic Molecules*, 1st. edn., Springer, Singapore, **2020**.

[13] a) H.-Y. Wong, W.-S. Lo, K.-H. Yim, G.-L. Law, *Chem* **2019**, *5*, 3058–3095; b) B. Doistau, J.-R. Jiménez, C. Piguet, *Front. Chem.* **2020**, *8*, 555.

[14] a) Y. Shi, P. Duan, S. Huo, Y. Li, M. Liu, *Adv. Mater.* **2018**, *30*, 1705011; b) X. Yang, X. Jin, T. Zhao, P. Duan, *Mater. Chem. Front.* **2021**, *5*, 4821–4832; c) J. Wade, J. R. Brandt, D. Reger, F. Zinna, K. Y. Amsharov, N. Jux, D. L. Andrews, M. J. Fuchter, *Angew. Chem. Int. Ed.* **2021**, *60*, 222–227; *Angew. Chem.* **2021**, *133*, 224–229; d) M. Kazem-Rostami, A. Orte, A. M. Ortuño, A. H. G. David, I. Roy, D. Miguel, A. Garci,

C. M. Cruz, C. L. Stern, J. M. Cuerva, J. F. Stoddart, *J. Am. Chem. Soc.* **2022**, *144*, 9380–9389.
[15] a) P. Reiné, J. Justicia, S. P. Morcillo, S. Abbate, B. Vaz, M. Ribagorda, Á. Orte, L. Álvarez de Cienfuegos, G. Longhi, A. G. Campaña, D. Miguel, J. M. Cuerva, *J. Org. Chem.* **2018**, *83*, 4455–4463; b) D. Parker, J. D. Fradgley, K.-L. Wong, *Chem. Soc. Rev.* **2021**, *50*, 8193–8213.
[16] L. E. MacKenzie, R. Pal, *Nat. Chem. Rev.* **2021**, *5*, 109–124.
[17] a) L. Cerdán, S. García-Moreno, A. Costela, I. García-Moreno, S. de la Moya, *Sci. Rep.* **2016**, *6*, 28740; b) W. Dai, Y. Wang, R. Li, Y. Fan, G. Qu, Y. Wu, Q. Song, J. Han, S. Xiao, *ACS Nano* **2020**, *14*, 17063–17070.
[18] D.-W. Zhang, M. Li, C.-F. Chen, *Chem. Soc. Rev.* **2020**, *49*, 1331–1343.
[19] a) S. Sato, A. Yoshii, S. Takahashi, S. Furumi, M. Takeuchi, H. Isobe, *Proc. Natl. Acad. Sci. U.S.A.* **2017**, *114*, 13097–13101; b) J. Wang, G. Zhuang, M. Chen, D. Lu, Z. Li, Q. Huang, H. Jia, S. Cui, X. Shao, S. Yang, P. Du, *Angew. Chem. Int. Ed.* **2020**, *59*, 1619–1626; *Angew. Chem.* **2020**, *132*, 1636–1643.
[20] a) M. Hu, H.-T. Feng, Y.-X. Yuan, Y.-S. Zheng, B. Z. Tang, *Coord. Chem. Rev.* **2020**, *416*, 213329; b) M.-M. Zhang, X.-Y. Dong, Z.-Y. Wang, H.-Y. Li, S.-J. Li, X. Zhao, S.-Q. Zang, *Angew. Chem. Int. Ed.* **2020**, *59*, 10052–10058; *Angew. Chem.* **2020**, *132*, 10138–10144; c) H. Shang, Z. Ding, Y. Shen, B. Yang, M. Liu, S. Jiang, *Chem. Sci.* **2020**, *11*, 2169–2174; d) K. Liu, Y. Shen, X. Li, Y. Zhang, Y. Quan, Y. Cheng, *Chem. Commun.* **2020**, *56*, 12829–12832; e) W.-J. Li, Q. Gu, X.-Q. Wang, D.-Y. Zhang, Y.-T. Wang, X. He, W. Wang, H.-B. Yang, *Angew. Chem. Int. Ed.* **2021**, *60*, 9507–9515; *Angew. Chem.* **2021**, *133*, 9593–9601.
[21] a) M. Hasegawa, Y. Nojima, Y. Mazaki, *ChemPhotoChem* **2021**, *5*, 1042–1058; b) Y. Morisaki, M. Gon, T. Sasamori, N. Tokitoh, Y. Chujo, *J. Am. Chem. Soc.* **2014**, *136*, 3350–3353; c) K. Takaishi, M. Yasui, T. Ema, *J. Am. Chem. Soc.* **2018**, *140*, 5334–5338; d) Y. Nojima, M. Hasegawa, N. Hara, Y. Imai, Y. Mazaki, *Chem. Commun.* **2019**, *55*, 2749–2752; e) H. Zhu, Q. Li, B. Shi, H. Xing, Y. Sun, S. Lu, L. Shangguan, X. Li, F. Huang, P. J. Stang, *J. Am. Chem. Soc.* **2020**, *142*, 17340–17345; f) Y. Nojima, M. Hasegawa, N. Hara, Y. Imai, Y. Mazaki, *Chem. Eur. J.* **2021**, *27*, 5923–5929; g) K. Sato, M. Hasegawa, Y. Nojima, N. Hara, T. Nishiuchi, Y. Imai, Y. Mazaki, *Chem. Eur. J.* **2021**, *27*, 1323–1329; h) M. Krzeszewski, H. Ito, K. Itami, *J. Am. Chem. Soc.* **2022**, *144*, 862–871.
[22] J.-B. Xiong, H.-T. Feng, J.-P. Sun, W.-Z. Xie, D. Yang, M. Liu, Y.-S. Zheng, *J. Am. Chem. Soc.* **2016**, *138*, 11469–11472.
[23] K. Li, H. Ji, Z. Yang, W. Duan, Y. Ma, H. Liu, H. Wang, S. Gong, *J. Org. Chem.* **2021**, *86*, 16707–16715.
[24] a) J. C. Barnes, M. Juríček, N. L. Strutt, M. Frasconi, S. Sampath, M. A. Giesener, P. L. McGrier, C. J. Bruns, C. L. Stern, A. A. Sarjeant, J. F. Stoddart, *J. Am. Chem. Soc.* **2013**, *135*, 183–192; b) E. J. Dale, N. A. Vermeulen, M. Juríček, J. C. Barnes, R. M. Young, M. R. Wasielewski, J. F. Stoddart, *Acc. Chem. Res.* **2016**, *49*, 262–273; c) A. Garci, J. A. Weber, R. M. Young, M. Kazem-Rostami, M. Ovalle, Y. Beldjoudi, A. Atilgan, Y. J. Bae, W. Liu, L. O. Jones, C. L. Stern, G. C. Schatz, O. K. Farha, M. R. Wasielewski, J. F. Stoddart, *Nat. Catal.* **2022**, *5*, 524–533; d) I. Roy, A. H. G. David, P. J. Das, D. J. Pe, J. F. Stoddart, *Chem. Soc. Rev.* **2022**, *51*, 5557–5605.
[25] A. Garci, Y. Beldjoudi, M. S. Kodaimati, J. E. Hornick, M. T. Nguyen, M. M. Cetin, C. L. Stern, I. Roy, E. A. Weiss, J. F. Stoddart, *J. Am. Chem. Soc.* **2020**, *142*, 7956–7967.
[26] I. Roy, S. Bobbala, J. Zhou, M. T. Nguyen, S. K. M. Nalluri, Y. Wu, D. P. Ferris, E. A. Scott, M. R. Wasielewski, J. F. Stoddart, *J. Am. Chem. Soc.* **2018**, *140*, 7206–7212.
[27] a) M. Asakawa, C. L. Brown, D. Pasini, J. F. Stoddart, P. G. Wyatt, *J. Org. Chem.* **1996**, *61*, 7234–7235; b) M. Asakawa, P. R. Ashton, S. E. Boyd, C. L. Brown, S. Menzer, D. Pasini, J. F. Stoddart, M. S. Tolley, A. J. P. White, D. J. Williams, P. G. Wyatt, *Chem. Eur. J.* **1997**, *3*, 463–481; c) P. R. Ashton, A. M. Heiss, D. Pasini, F. M. Raymo, A. N. Shipway, J. F. Stoddart, *Eur. J. Org. Chem.* **1999**, 995–1004.
[28] a) S. S. Peacock, D. M. Walba, F. C. A. Gaeta, R. C. Helgeson, D. J. Cram, *J. Am. Chem. Soc.* **1980**, *102*, 2043–2052; b) L. Pu, *Chem. Rev.* **1998**, *98*, 2405–2494.
[29] a) X. Zhang, Y. Zhang, H. Zhang, Y. Quan, Y. Li, Y. Cheng, S. Ye, *Org. Lett.* **2019**, *21*, 439–443; b) A. Nitti, D. Pasini, *Adv. Mater.* **2020**, *32*, 1908021; c) C. Liu, J.-C. Yang, J. W. Y. Lam, H.-T. Feng, B. Z. Tang, *Chem. Sci.* **2022**, *13*, 611–632.
[30] Deposition numbers 2160991 and 2167998 contain the supplementary crystallographic data for this paper. These data are provided free of charge by the joint Cambridge Crystallographic Data Centre and Fachinformationszentrum Karlsruhe Access Structures service.
[31] a) L. de Thieulloy, L. Le Bras, B. Zumer, J. Sanz García, C. Lemarchand, N. Pineau, C. Adamo, A. Perrier, *ChemPhysChem* **2021**, *22*, 1802–1816; b) L. Le Bras, C. Adamo, A. Perrier, *J. Phys. Chem. C* **2017**, *121*, 25603–25616.
[32] R. Englman, J. Jortner, *Mol. Phys.* **1970**, *18*, 145–164.
[33] The sign of the signal and the g_{lum} values are also consistent with the sign and the g_{abs} values of the lowest energy absorption transition for each compound. This correlation has been shown by Mori and co-workers: H. Tanaka, Y. Inoue, T. Mori, *ChemPhotoChem* **2018**, *2*, 386–402.
[34] Note that the CPL spectra of both sets of enantiomers in the aggregated state are reproducible. They were performed twice with different samples of the compounds, affording similar results. See Figures S72 and S74.
[35] P. M. L. Blok, H. P. J. M. Dekkers, *Appl. Spectrosc.* **1990**, *44*, 305–402.
[36] For examples of CPL responses in the solid state exhibiting different magnitude depending on the enantiomer, see: a) W. Duan, K. Li, H. Ji, Y. Huo, Q. Yao, H. Liu, S. Gong, *Dyes Pigm.* **2021**, *193*, 109538; b) Q. Cheng, A. Hao, P. Xing, *ACS Nano* **2022**, *16*, 6825–6834; c) H.-T. Feng, X. Gu, J. W. Y. Lam, Y.-S. Zheng, B. Z. Tang, *J. Mater. Chem. C* **2018**, *6*, 8934–8940; d) L. Wang, N. Suzuki, J. Liu, T. Matsuda, N. A. A. Rahim, W. Zhang, M. Fujiki, Z. Zhang, N. Zhou, X. Zhu, *Polym. Chem.* **2014**, *5*, 5920–5927.

Manuscript received: June 13, 2022
Accepted manuscript online: July 29, 2022
Version of record online: August 22, 2022